ADVANCED FUNCTIONAL MATERIALS
www.afm-journal.de

Engineering a Spin-Orbit Bandgap in Graphene-Tellurium Heterostructures

Beatriz Muñiz Cano, Fabián Calleja, Daniela Pacilè, Marc G. Cuxart, Michele Pisarra, Antonello Sindona, Fernando Martín, Elena Salagre, Pilar Segovia, Enrique G. Michel, Amadeo. L. Vázquez de Parga, Rodolfo Miranda, Julio Camarero, Manuela Garnica, and Miguel Angel Valbuena**

Intensive research has focused on harnessing the potential of graphene for electronic, optoelectronic, and spintronic devices by generating a bandgap at the Dirac point and enhancing spin-orbit interaction. While proximity to heavy *p* elements is promising, their interaction in graphene heterostructures remains underexplored compared to ferromagnetic, noble, or heavy metals. This study demonstrates the effective intercalation of Te atoms in a graphene/Ir(111) heterostructure. Using low-energy electron diffraction and scanning tunneling microscopy, two distinct structural phases are identified as a function of Te coverage. Angle-resolved photoemission spectroscopy reveals a 240 meV bandgap at the Dirac cone at room temperature, preserving linear dispersion, along with a pronounced n-doping effect confirmed by quasiparticle interference maps. Notably, reducing Te coverage tunes the Dirac point toward the Fermi level while maintaining the bandgap. Spin-resolved measurements uncover a non-planar chiral spin texture with significant splitting in both in-plane and out-of-plane components, as well as evidence of an emerging edge state from scanning tunneling spectroscopy. These findings highlight Te-enhanced intrinsic spin-orbit coupling in graphene, surpassing the extrinsic Rashba effect and promoting a spin-orbit-induced bandgap. This system offers a promising platform for spin-dependent transport phenomena, such as the quantum spin Hall effect.

1. Introduction

Since the discovery of the unique properties of graphene (Gr) such as its high electron and hole mobilities,[1,2] the long spin lifetime and long-distance spin propagation at room temperature (RT),[3] or its high electrical conductivity,[4] research into its properties has experienced a great increase. The Gr electronic structure is characterized by its π valence band, which is half filled and degenerate at the $\overline{K}_{Gr}$ point exactly at the Fermi level (E_F), the so-called Dirac point (DP). In the vicinity of the DP its band structure follows a linear relativistic-like dispersion described by the Dirac equation. In spite of these exceptional features, the application of Gr to electronic, spintronic or spinorbitronic devices[5–8] has been jeopardized by the fact that pristine Gr lacks a bandgap, which makes it difficult to control certain technologically relevant processes such as on-off switching operations in transistors.[9]

B. M. Cano, F. Calleja, M. G. Cuxart, M. Pisarra, F. Martín, A. L. Vázquez de Parga, R. Miranda, J. Camarero, M. Garnica, M. A. Valbuena
Instituto Madrileño de Estudios Avanzados, IMDEA Nanociencia, Calle Faraday 9
28049 Madrid, Spain
E-mail: manuela.garnica@imdea.org; miguelangel.valbuena@imdea.org

D. Pacilè, M. Pisarra, A. Sindona
INFN, sezione LNF, Gruppo collegato di Cosenza, Cubo 31C
I-87036 Rende (CS), Italy

A. Sindona
Departamento de Química, Módulo 13
Universidad Autónoma de Madrid
28049 Madrid, Spain

F. Martín
Departamento de Física de la Materia Condensada
Universidad Autónoma de Madrid (UAM), Campus de Cantoblanco
28049 Madrid, Spain

E. Salagre, P. Segovia, E. G. Michel, A. L. Vázquez de Parga, R. Miranda, J. Camarero
Condensed Matter Physics Center (IFIMAC)
Universidad Autónoma de Madrid (UAM), Campus de Cantoblanco
28049 Madrid, Spain

P. Segovia, E. G. Michel, A. L. Vázquez de Parga, R. Miranda, J. Camarero
Instituto Universitario de Ciencia de Materiales "Nicolás Cabrera"
Universidad Autónoma de Madrid
28049 Madrid, Spain

The ORCID identification number(s) for the author(s) of this article can be found under https://doi.org/10.1002/adfm.202425154

DOI: 10.1002/adfm.202425154

Three main mechanisms have been explored to induce the desired bandgap in Gr, namely: i) the imposition of a superperiodicity on the Gr lattice, leading to confinement effects;[10–14] ii) the breaking of the sublattice symmetry and the subsequent generation of a lattice mismatch;[15–20] and iii) the development of a sufficiently strong spin-orbit interaction (SOI).[21–24]

In this regard, some technologically significant quantum states,[25] such as the quantum spin Hall (QSH) effect,[26] require not only the opening of a gap, but also the sublattice symmetry not to be broken, thus preserving time-reversal symmetry (TRS). The QSH phase is a two-dimensional (2D) topological insulator state, which has been predicted to be achievable in Gr.[27–29] In this context, the SOI must be taken into account for the generation of a bandgap. When the SOI is strong enough, the bulk bandgap of Gr is inverted, allowing for the realization of a topologically non-trivial state. If the strength of the intrinsic SOI is larger than the Rashba SOI, according to Kane and Mele's prediction, a bandgap appears at the Gr DP. Nevertheless, the intrinsic spin-orbit splitting of pristine Gr is extremely weak and, unavoidably, overcome by the Rashba SOI,[30–34] resulting in an insignificantly small energy gap.[35,36]

Different routes have been pursued to enhance the SOI in Gr and, therefore, to promote the spin-orbit gap. For instance, proximity effects with layered 2D SOI materials, such as transition metal dichalcogenides (TMDs), topological insulators, or magnetic layers, have been explored.[37–40] Another prominent example of significant relevance involves attempts to induce strong hybridization with an intercalated heavy metal (HM).[41,42] Particularly, much research has been devoted to 5*d* HM intercalation.[43–46] However, these kind of metals (such as Au or Ir) only increase the Rashba spin splitting of the electronic states.[47–49] Hybridization with 4*f* intercalated magnetic layers, such as Eu, can also induce a significant bandgap in the free-standing Dirac cone dispersion, accompanied by a lifting of spin degeneracy due to the mixing of Gr and Eu states.[50]

One of the most successful cases for enhancing the SOI and generating the spin-orbit gap has been the intercalation of *p* outer shell HMs,[51] as Pb on Gr/Pt(111)[21] or Gr/Ir(111).[22] In Gr/Pb/Ir(111) the extrinsic SOI continued to overcome the intrinsic one, and no gap opening was observed. In the case of Gr/Pb/Pt(111), a surpassing of the extrinsic SOI was achieved, resulting in the opening of a spin-orbit gap. On the contrary, similar *p* orbital HMs intercalation, as Bi on Gr/Ir(111),[18] do not promote any sizeable SOI effects in Gr and the observed gap opening at the DP has been related to the breaking of the sublattice symmetry, which prevents this system to be used as a platform for the implementation of the QSH effect.

Thus, while 5*d* or 4*f* HMs have been extensively studied, the influence of the last *p*-filled shell elements remains less explored. Continuing the trend of previously investigated elements such as Pb and Bi, as well as Sn[52] and Sb,[53] this work focuses on the electronic structure of Te-intercalated Gr/Ir(111) heterostructures, following the band filling sequence of outer *p* shell elements. Moreover, Te is well-known for introducing significant SOI in 2D layered materials.[54] Exploring this pathway offers valuable insights into the interactions between chalcogen atoms and Gr supporting substrate, paving the way for engineering novel 2D materials, such as TMD monolayers (ML) and other van der Waals (vdW) heterostructures with tailored properties.[38,55–57]

In the first part of this work, low energy electron diffraction (LEED) and scanning tunneling microscopy (STM) are used to demonstrate how the Te intercalation process can be successfully performed in Gr/Ir(111). Two long-range ordered structural phases are unveiled depending on the intercalated Te coverage. In the second part, the effects induced in the Gr electronic structure by the intercalated Te phases are also elucidated by means of scanning tunneling spectroscopy (STS), angle-resolved photoemission spectroscopy (ARPES), spin-resolved ARPES (SR-ARPES) and density functional theory (DFT) calculations. Particularly significant is the emergence of a substantial bandgap at the DP at RT extending up to 240 meV and its tuning with the Te coverage. Interestingly, at low Te coverage the bandgap persists, and Gr becomes nearly charge neutral, in such a way that the E_F is tuned into the gap. The SR-ARPES measurements reveal a significant energy spin-splitting, while STM measurements demonstrate the emergence of an edge state, both supporting the intrinsic SOI as the origin of the induced bandgap and suggesting that transport properties near the DP are dominated by charge carriers with a single spin component. These findings open viable routes for the development of electronic and spintronic devices based on Gr/Te heterostructures.

2. Results and Discussion

2.1. Structural Characterization

The samples were prepared in three steps, as described in more details in the Experimental Section. First, a Gr ML was grown on an Ir(111) single crystal by chemical vapor deposition. The LEED pattern, exhibiting the expected moiré structure, is presented in Figure S1a (Supporting Information). Second, different amounts of Te were evaporated on Gr/Ir(111), promoting the formation of Te islands. As a result, the moiré spots were suppressed, and several concentric circles indicating the multiple domains of the Te islands appear at the selected electron beam energy (80 eV, Figure S1b, Supporting Information). Finally, annealing the samples at 473 K resulted in the effective intercalation of Te between Gr and the underlying Ir(111) substrate.

Two distinct samples were prepared, each leading to a different Te-coverage-dependent phase, obtained by controlling the Te evaporation and exposure time. The LEED patterns corresponding to these phases are shown in **Figure 1**a,e. Both images display different spot distributions compared to those in Figure S1a,b (Supporting Information), indicating complete Te intercalation and the formation of a superstructure of Te on Ir(111). Notably, the LEED pattern in Figure 1a exhibits a residual moiré pattern, suggesting a slight reduction in the decoupling of Gr from the substrate. This can be attributed to the lower concentration of Te, as opposed to the higher coverage phase, where no moiré pattern is observed. Also, models of the real space structures associated with such patterns are presented in Figure 1b,f, correspondingly. Thus, two different regimes are identified, namely, a $(\sqrt{3} \times \sqrt{3})R30°$ phase (Figure 1a,b), and a series of alternated periodic repetitions of a c(4 × 2) reconstruction in which the maximum number of Te atoms is accommodated (Figure 1e,f).

In a preliminary estimation of the density of Te atoms extracted from the real space structure, Te/Ir ratios of 1/3 ML and of 4/9

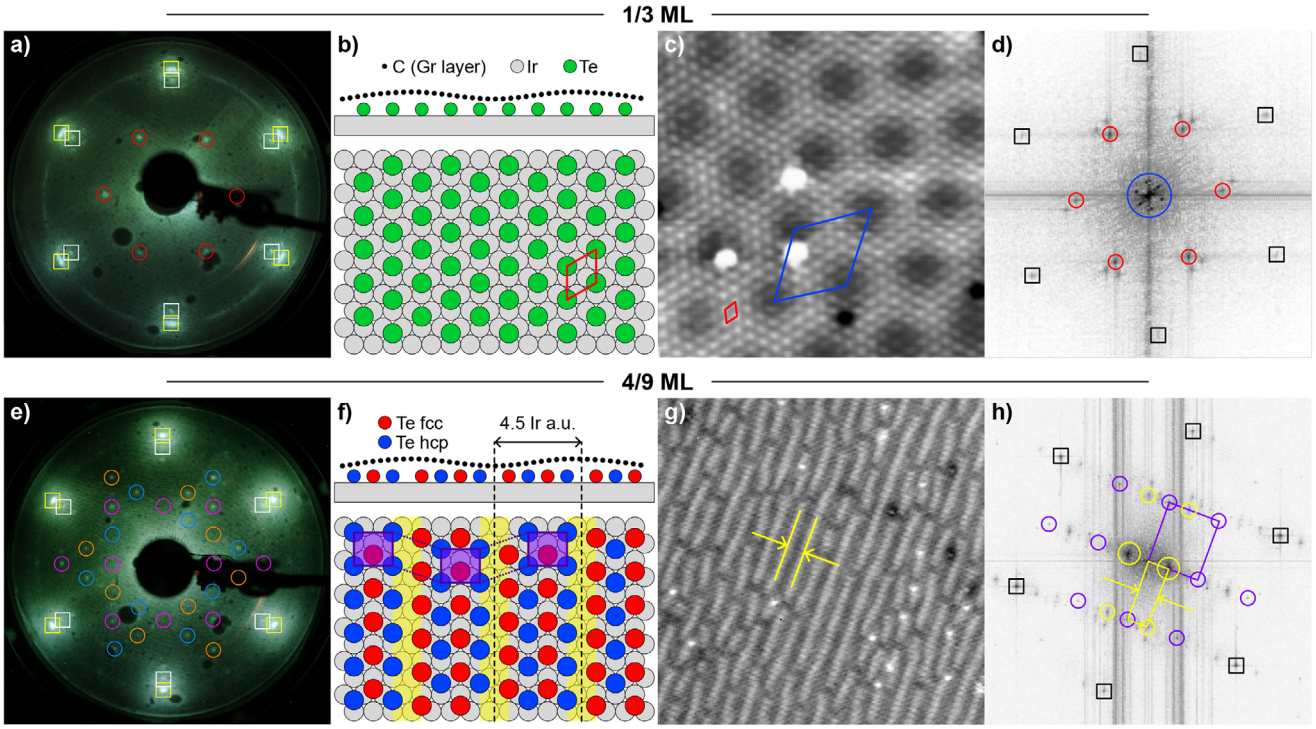

Figure 1. LEED and STM characterization of the Te-intercalated Gr/Ir(111) heterostructures revealing two different structral phases depending of the amount of intercalated Te. Top panels: 1/3 ML phase. a) LEED pattern showing a pure $(\sqrt{3} \times \sqrt{3})$R30° reconstruction. Graphene, Ir, and Te spots are highlighted by yellow squares, white squares and red circles, respectively. The corresponding real space model is provided in (b). c) 9 nm crop of a 15 nm side HR-STM image (V_b=2 V, I_t=0.35 nA). The moiré pattern unit cell and the one created by the Te structure are depicted in blue and red, respectively. d) FFT of the complete image presented in (c), showing the Te $(\sqrt{3} \times \sqrt{3})°$ structure (red circles). The atomic lattice of Gr and the Gr/Ir moire pattern are indicated by black squares and a blue circle, respectively. Bottom panels: 4/9 ML phase. e) LEED pattern and f) associated real space model showing a reconstruction (whose three different domains are superimposed in blue, magenta, and orange on top of the LEED) consisting in a series of alternated periodic repetitions of a c(4x2) reconstruction in which the maximum number of Te atoms is accommodated. The c(4x2) unit cell is highlighted in purple in the model presented in (f), where the yellow rectangles indicate the areas which give rise to the quasi-one dimensional stripes observed in the STM experiments, separated by 4.5 Ir atomic units (a.u.). g) 25 nm crop of a 45 nm side HR-STM image (V_b=0.57 V, I_t =0.5 nA). The stripe pattern is highlighted by the pair of yellow lines. h) FFT corresponding to the complete image presented in (g), showing simultaneously a single domain of the c(4x2) periodicity present in the LEED pattern of panel (e) (here highlihted in purple), as well as the stripe pattern described in (f) (highlighted in yellow). LEED patterns have been acquired at E = 80 eV. In the real space models, grey circles represent Ir atoms and green ones stand for Te in (b), where the red rhomboid depicts the unit cell of the structure. In (f), both red and blue circles represent Te in fcc and hcp positions with respect to the Ir surface, respectively (see Section SV, Supporting Information).

ML are found, which is the notation we will refer to from here onwards. In all reconstructions, Te atoms (in green in Figure 1b and in both red and blue in Figure 1f, see figure caption for more details) have been placed at threefold on-hollow sites with respect to the Ir lattice since these are the most energetically favorable adsorption sites (see Section SV, Supporting Information). The same structural configuration has been predicted in similar systems.[58–60]

A high-resolution (HR-) STM topographic image of the 1/3 ML sample acquired in one of the Te-intercalated areas is shown in Figure 1c. A characteristic large scale STM image is included in Figure S2a (Supporting Information), whose profile along the black line (displayed in the lower panel) reveals different flat areas with a step height associated to Ir atomic terraces (2.2 Å) and small patches with a height compatible with Te intercalation (1.6 Å), in the latter of which Figure 1c was acquired. Both Figure 1c and its corresponding fast Fourier transform (FFT) image (Figure 1d) reveal how the Te atoms are arranged in a $(\sqrt{3} \times \sqrt{3})$R30° reconstruction, in agreement with the LEED pattern shown in Figure 1a.

In the 4/9 ML sample, most of the surface shows a set of quasi-one dimensional stripes oriented in three preferential directions (see Figures S2b and S3b, Supporting Information). A HR-STM image recorded on one of such domains and its corresponding FFT pattern are shown in Figure 1g,h, respectively. The absence of the moiré pattern and the fact that the Gr can be clearly resolved indicate that the Te is intercalated. The separation between the stripes is of (1.3 ± 0.1) nm ≈ 4.5 Ir atomic units (a.u.). This value is in good agreement with the real space model represented in Figure 1f. The same consistency is found between the remaining STM findings, as compared to the conclusions previously drawn from the LEED characterization.

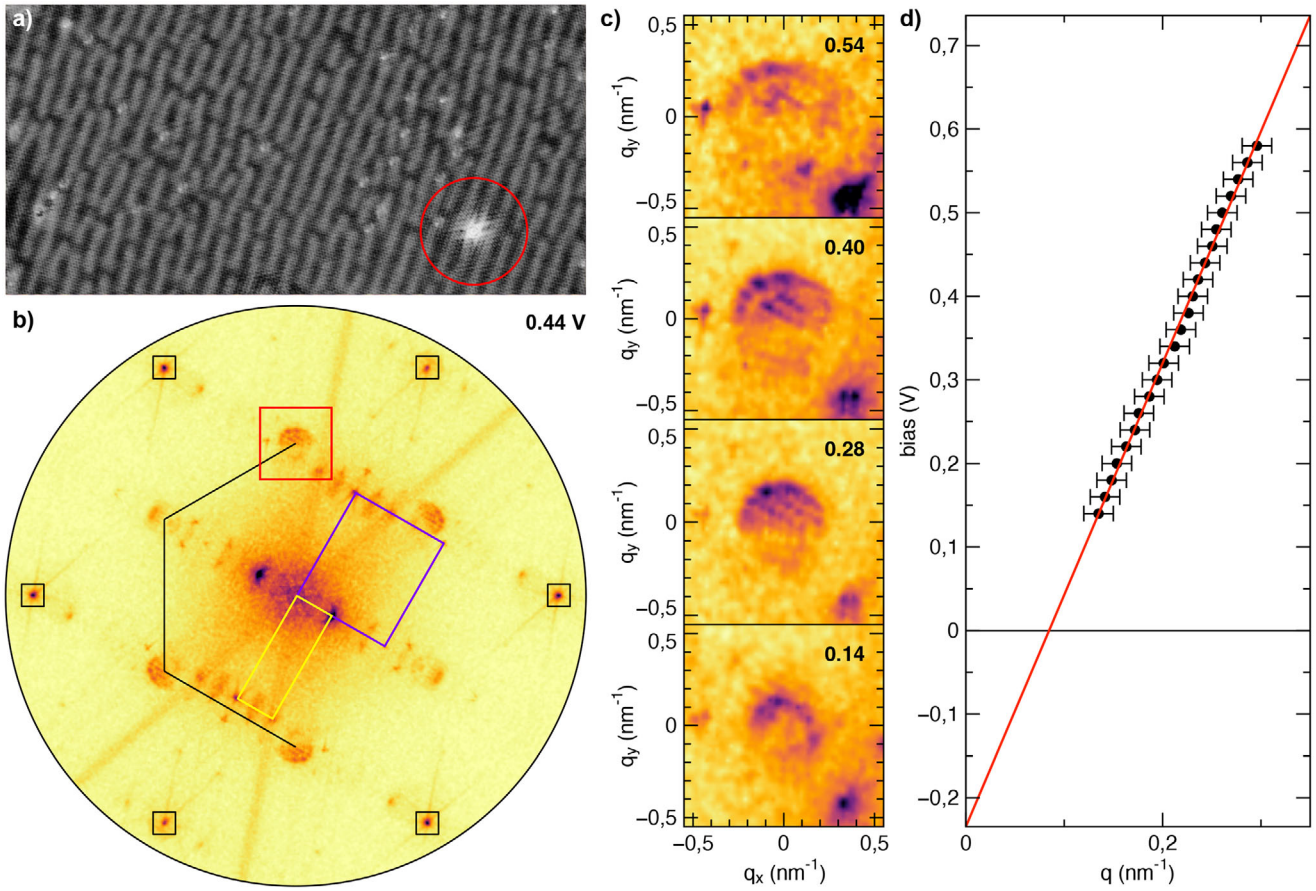

Figure 2. QPIs analysis. a) HR-STM image (V_b=200 mV, I_t=0.5 nA) corresponding to a Te-intercalated area in the 4/9 ML sample, revealing intervalley scattering signatures around the point defects (see red circle), appearing as a consequence of the decoupling induced by the Te intercalation. b) FFT image of an dI/dV map taken at 0.44 V. The spots from Gr atomic lattice are highlighted by black squares, and the corresponding SBZ is marked with black lines (halve of it). In addition to the c(4x2) and stripe signals already explained in Figure 1 (highlighted here in purple and yellow, respectively), a clear inter-valley signal can be appreciated at the corners of the SBZ (see red square). c) Zoom in to the SBZ corner highlighted in red in (b), presenting four energy slices from a dI/dV bias series ranging from 0.14 to 0.54 V. The bias voltage of each slice is presented in the top right corner, in volts. d) Dispersion relation obtained from the complete bias series by performing a radial average of the inter-valley signal centered at the SBZ corner. The red line is a linear fit yielding a DP energy of –0.23 eV. All measurements have been taken at 1.2 K.

2.2. Electronic Structure Characterization

The Gr layer remains completely decoupled from the Ir metallic substrate once the Te has intercalated, regardless of the Te intercalation coverage. This decoupling is evidenced by the observation of scattering patterns around defects in HR-STM images.[61,62] **Figure 2** shows a region of the 4/9 ML phase, where the previously described stripe pattern and several defects are visible. Notably, a flower-shaped defect (marked with a red circle in Figure 2a) and several point defects stand out. The flower defects, featuring a central ring surrounded by a six-fold symmetric structure, are likely induced by the heating during the intercalation process.[63] Surrounding the defects, a $(\sqrt{3} \times \sqrt{3})$R30° pattern appears relative to the Gr lattice, which is attributed to intervalley scattering between the K and K′ states.[64] As reported before[62,65,66] and shown in Figure 2, the analysis of these modulations provide detailed information on the electronic structure of the material under study. The scattering vector q is energy dependent and can be extracted from the FFT of spectroscopic dI/dV maps of the STM images as in Figure 2, the so-called quasiparticle interference (QPI) maps. In the case of Gr, intervalley scattering results in a ring centered at the corners of its surface Brillouin zone (SBZ), with a radius of $2k_F$, as observed in the Figure 2b. This ring arises from scattering between states at $\vec{k}_F$ and $-\vec{k}_F$. Figure 2c depicts the energy dispersion from the analysis of the q vector in a series of FFT from 120 mV to 580 mV. From the fitting of the experimental data (red line in Figure 2d), is concluded that the DP energy is at (–230 ± 80) mV and the Fermi velocity is $(1.0 \pm 0.1) \cdot 10^6$ m s^{-1}. A clear n-doping of the system is then observed as a result of a charge transfer between Gr and Te, however, from the electronic point of view, Gr can be considered close to quasi-free-standing.

A systematic ARPES study using He I radiation was conducted to characterize the evolution of the band structure of the two Gr/Te/Ir(111) phases at RT. HR-ARPES spectra of the two representative samples (1/3 ML and 4/9 ML) at the Dirac cones, just

below the E_F, are displayed in **Figure 3a,c**. The measurements were acquired at the $\overline{K}_{Gr}$ point along the perpendicular direction to $\overline{\Gamma K}$ (as schematically depicted in the insets). ARPES spectra showing the Dirac cone band dispersion of the Gr/Ir(111) reference system are provided in Figure S10 (Supporting Information) for comparison. The overall band structures in an energy range spanning from the E_F to the bottom of the Gr π band are included in Figure S5 (Supporting Information), in which the band structure of an even lower Te coverage sample can also be found. Gr π bands are sharp and intense, which indicates an optimal structural and interfacial quality. No signs of the Gr π band replicas arising from the moiré pattern can be appreciated (except from the bandmap corresponding to the lower coverage in Figure S5c,f, Supporting Information), something that, in conjunction with the subsequent absence of avoid-crossing mechanism bandgaps, confirm an effective Gr decoupling from the Ir(111) substrate due to the Te intercalation. Most importantly, the ARPES bandmaps in Figure 3a,c reveal the emergence of a bandgap at the DP in both of the studied phases.

To characterize such a bandgap opening and the induced n-type doping, the energy distribution curves (EDCs) are presented in Figure 3b,d. Here, the opening of a bandgap at the DP, as well as its shifting towards higher binding energies (BE) with respect to Gr/Ir(111) are evident. Also, the quasi-free-standing character of the Gr π band is proved with an estimated group velocity, obtained from $1/\hbar(\partial E/\partial k)$,[67] of $(0.98 \pm 0.04)\cdot 10^6$ m s^{-1} in agreement with the STM data and comparable to the reported values for Gr/Ir(111), of $0.95\cdot 10^6$ m s^{-1},[68] or free-standing Gr, of 10^6 m s^{-1}.

The width of the bandgap E_G, estimated as the difference between the two maxima associated with the π and π* bands, amounts to (240 ± 80) meV and (180 ± 80) meV for increasing Te coverage. Notably, the energies of the DP are (260 ± 80) meV and (340 ± 80) meV, respectively, for the same Te coverage increase. Within the experimental error, this agrees with the value extracted from the FFT analysis for high Te coverage, demonstrating that controllable n-type doping of the system can be achieved while, most importantly, preserving the bandgap and the linear dispersion for both studied phases.

In order to investigate whether the bandgap is tunable up to the E_F, an even lower Te coverage sample was studied after reducing the Te evaporation dose. This sample exhibits the same LEED pattern as in Figure 1a. Figure S5c,f (Supporting Information) demonstrate how this sample is almost charge neutral, with the DP close to the E_F. The bandgap can be better revealed by a small n-type doping through Na alkali deposition on top of Gr. As shown in Figure S6 (Supporting Information), the bandgap is preserved and its energy can be consequently tuned backwards by such an electronic charge transfer.

A DFT adsorption study of Gr on several partially Te covered Ir surfaces was performed. In order to keep the size of the computations manageable, a stretched Gr layer was placed on two different Te covered Ir(111) surfaces so that the Gr lattice vectors match the Ir(111) lattice vectors, namely the $(\sqrt{3}\times\sqrt{3})°$, characterized by a 1/3 ML Te coverage; and the perfectly 2D periodic c(4 × 2) reconstruction, characterized by a 1/2 ML Te coverage (see the Experimental Section, and Section SV, Supporting Information, for more details). In both cases, the structural optimizations evidence that the Gr-substrate interaction has a dispersive nature, with the C atoms stabilized at a ≈3.5 Å vertical distance from the Te atoms. As for the electronic properties, upon inspection of the band-unfolded and Gr projected band structure in Figures S8 and S9 (Supporting Information), the Gr band dispersion is found to be almost unaffected by the presence of the substrate that, however, induces a significant n-type doping. A closer look shows that Gr-substrate band hybridization is present in several places, as shown by the band splitting of the Gr derived bands, even though the linear dispersion of the π bands is preserved in the vicinity of the $\overline{K}_{Gr}$ point. In **Figure 4a** zoom-in close to the $\overline{K}_{Gr}$ point and the E_F for the band structure of the two investigated intercalation regimes is reported. Here, the vertex of the Dirac cone is clearly downward shifted by ≈470 meV and ≈520 meV for the $(\sqrt{3}\times\sqrt{3})°$ and c(4 × 2) reconstructions, respectively, in fairly good agreement with the experimental results. A small band gap is opened at the Dirac cone in both cases. For the $(\sqrt{3}\times\sqrt{3})°$ a very small ≈6 meV gap is found, not visible in Figure 4a. For the c(4 × 2) a ≈28 meV gap is spotted in Figure 4b Additional considerations on the bandgap opening from calculations with spin-orbit coupling can be found in Section SV (Supporting Information). Thus, while DFT calculations account for electronic effects such as the n-type doping and electronic hybridization states, the bandgap magnitude is not fully reproduced. The gap observed in the DFT calculations arises from sublattice symmetry breaking effects introduced by the structural approximation used in the model, resulting in a value that is an order of magnitude smaller than the SOi-induced experimental bandgap.

2.3. Spin-Resolved Electronic Characterization

SR-ARPES measurements (see Experimental Section) on the 4/9 ML Te phase near the DP were performed with a mini-Mott detector to investigate potential energy spin-splitting and explore an SOI-related origin of the bandgap opening. Measurements were acquired with $h\nu = 21.2$ eV and at RT at an emission angle slightly off the $\overline{K}_{Gr}$ point of the Gr SBZ, corresponding to the Fermi wave vector denoted as K_{Gr}^{off}, as indicated in the experimental Fermi surface (FS) in **Figure 5a** and in the ARPES bandmap in Figure 5c by the purple dashed vertical and slanting lines, respectively. The FS exhibits the characteristic trigonal symmetry of quasi-freestanding Gr on Ir(111) with pronounced matrix element effects. The spin-up and spin-down components (Figure 5e–g) were extracted from the raw spin-resolved energy distribution curves (SR-EDCs) (see Figure S7, Supporting Information) using Equations (2) and (3) in the Experimental Section. The accuracy of the energy spin splitting estimated is limited by the acquired statistics, not the instrumental resolution, with a statistical error of ± 10 meV from the SR-EDC fitting.

Two orthogonal in-plane spin components, Sx' and Sy', were measured using the incorporated spin rotator lens system, which rotates the in-plane spins by ± 45° (see Figure 5b, Figure S7, Supporting Information, and Experimental Section). The S_z out-of-plane spin component was measured in both configurations. Remarkably, the Sx' in-plane and Sz out-of-plane spin components (Figure 5e,g) exhibit energy spin splittings larger than the fitting error, amounting to 30 and 50 meV for the π and π* bands in Sx',

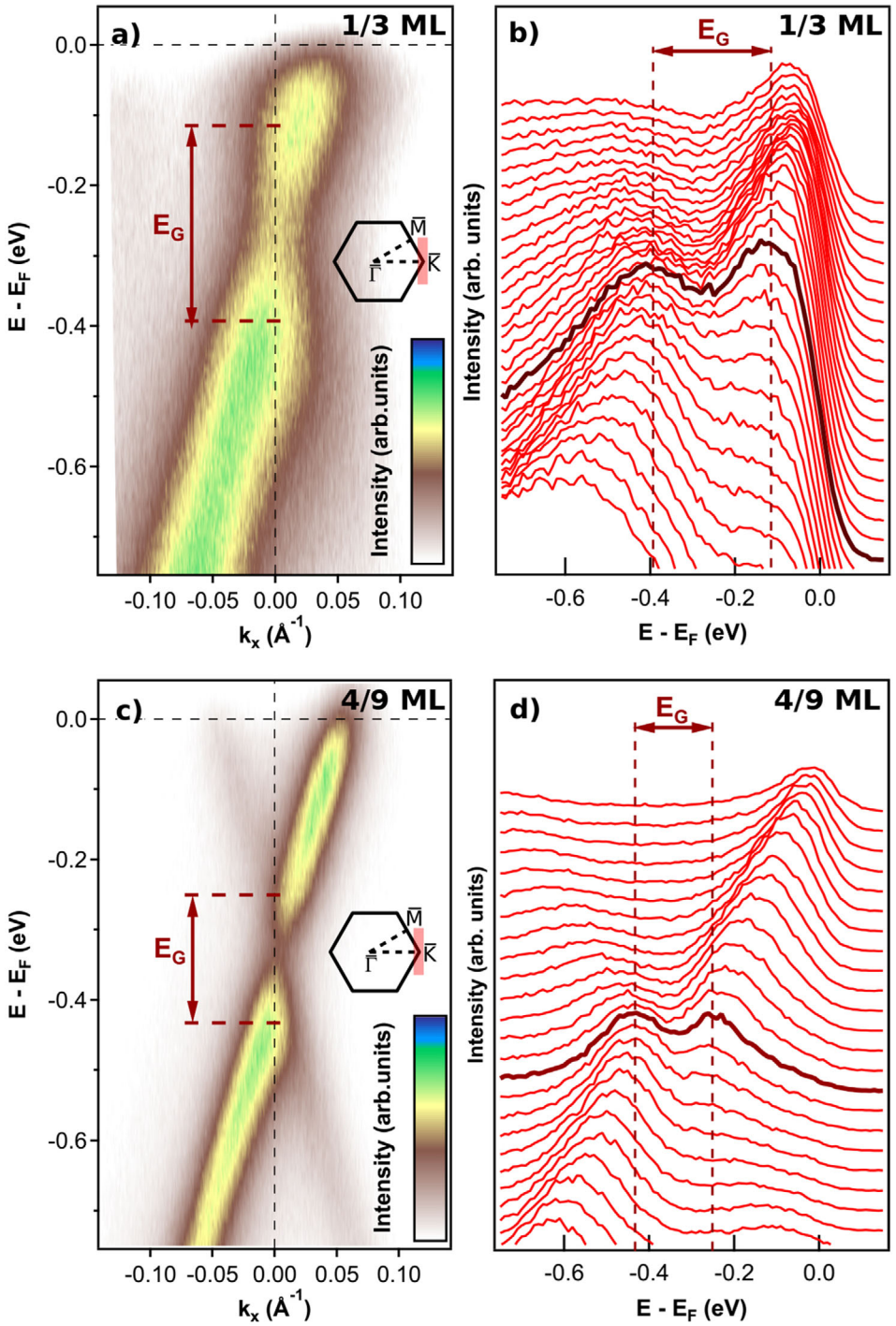

Figure 3. ARPES study on the Te-coverage dependence of the Dirac cone in the DP vicinity ($h\nu = 21.2$ eV and RT). ARPES bandmaps measured at the $\overline{K}_{Gr}$ point along the $\overline{\Gamma K}$ perpendicular direction for the a) 1/3 ML and c) 4/9 ML Te samples, as indicated by the SBZ sketches in panels (a) and (c). EDCs for the b) 1/3 ML and d) 4/9 ML Te samples obtained from (a) and (c), respectively. Dark red EDCs correspond to the $\overline{K}_{Gr}$ point. An energy shift of the DP away from the E_F as the Te coverage is increased is observed with values of, accordingly, (260 ± 80) meV and (340 ± 30) meV. The width of the bandgap E_G amounts for (240 ± 80) meV and (180 ± 80) meV for the 1/3 ML and 4/9 ML Te phases, respectively.

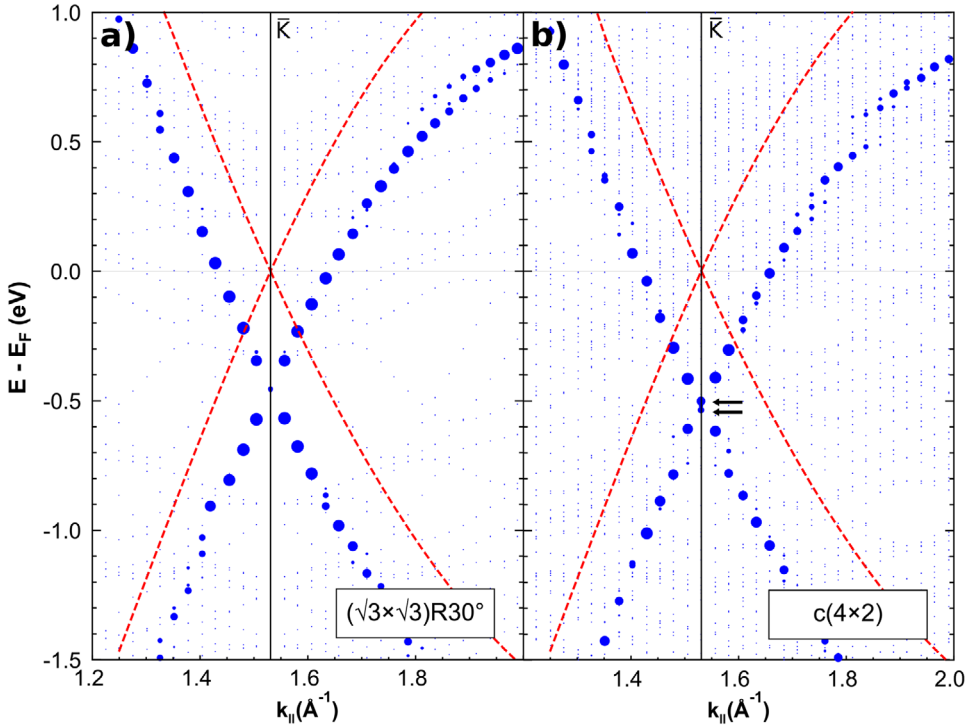

Figure 4. DFT Computed Band Structure near the DP. a) Band-unfolded and Gr-projected band structure near the $\bar{K}_{Gr}$ point and the Fermi level for the $(\sqrt{3}\times\sqrt{3})^{\circ}$ geometry, corresponding to a 1/3 ML Te coverage. A 6 meV (not visible) gap is found at the $\bar{K}_{Gr}$ point. b) Same as (a) for the perfectly periodic c(4 × 2) geometry, corresponding to a 1/2 ML Te coverage. A double point with high weight, which shows that a ≈28 meV gap (black arrows) is opened at the vertex of the Dirac cone, can be observed at the $\bar{K}_{Gr}$ point.

and 40 meV for both bands in S*z*. In contrast, the $S_{y'}$ in-plane spin component (Figure 5f) shows an energy splitting comparable to the fitting error.

These experimental findings are, to a first approximation, consistent with a non-planar quasi-chiral spin texture at the FS and the vicinity of the DP, as schematically depicted in Figure 5b. The spin texture combines a positive out-of-plane spin polarization (blue) with an anticlockwise quasi-chiral in-plane spin component (fuchsia arrow). This observation aligns with previous studies on similar heterostructures, such as *p* outer shell HMs as Pb intercalated between Gr and Pt or Ir(111).[21,22] In these systems, Pb intercalation promotes both extrinsic Rashba and intrinsic Kane–Mele SOI, leading to comparable energy spin splittings for in-plane and out-of-plane spin components near the DP. Similarly, the in-plane and out-of-plane spin splittings observed in Te-intercalated Gr suggest the induction of Rashba (extrinsic) and Kane–Mele (intrinsic) SOI, respectively. Since a bandgap is observed at the DP in both Te-intercalated phases, it is likely that the intrinsic SOI contribution dominates over the Rashba effect, resulting in a SOI-induced bandgap, as seen in Pb-intercalated Gr/Pt(111).[21] Similarly, the spin-resolved measurements reveal both in-plane and out-of-plane spin polarizations in Te-intercalated Gr. This observation is consistent with the presence of both Rashba-type (extrinsic) and intrinsic SOI contributions: Rashba SOI typically leads to in-plane spin splitting, while intrinsic SOI, such as that described by the Kane–Mele model, results in out-of-plane spin polarization near the Dirac point. Since a bandgap is observed at the DP in both Te-intercalated phases, it is likely that the intrinsic SOI contribution dominates over the Rashba effect, resulting in a SOI-induced bandgap, as seen in Pb-intercalated Gr/Pt(111).[21]

The experimental band dispersion, bandgap, and energy spin splitting can be modeled using the Hamiltonian describing relativistic Dirac electrons in Gr near the $\bar{K}_{Gr}$ point (Figure 5d). While the full Hamiltonian for proximized Gr is complex and challenging to handle (see, e.g., refs. [37,40]) it can be simplified for the studied Te-intercalated systems (and similarly for Pb)[21] due to the preservation of linear dispersion, Fermi velocity, and the submonolayer coverage of intercalated Te. Thus, a Hamiltonian including only the low-energy term (H_0), intrinsic SOI (H_{int}, Kane and Mele),[27] and extrinsic SOI (H_{ext}, Rashba)[30] serves as a realistic approximation[69,70] (see Equation S1 in Section SVI, Supporting Information, for details).

The eigenvalues of the considered Hamiltonian (Equation S1, Supporting Information) near the $\bar{K}_{Gr}$ point are given by:

$$E_{\mu,\nu} = E_{DP}(\nu) + \mu \cdot \lambda_{ext} + \\ +\nu \cdot \sqrt{(\hbar v_F k)^2 + (\lambda_{ext} - \mu\lambda_{int})^2} \quad (1)$$

where $\mu, \nu = \pm 1$ correspond to different spin chiralities and to valence and conduction bands, respectively; $E_{DP}(\nu)$ to the energy of the DP, which depends on the chiral channel ν; and the wave vector k is given relative to the $\bar{K}_{Gr}$ point. In accordance with Kane and Mele's model, a bandgap can be developed if the intrinsic SOI is larger than the Rashba one, i.e., $|\lambda_{int}| > |\lambda_{ext}|$.

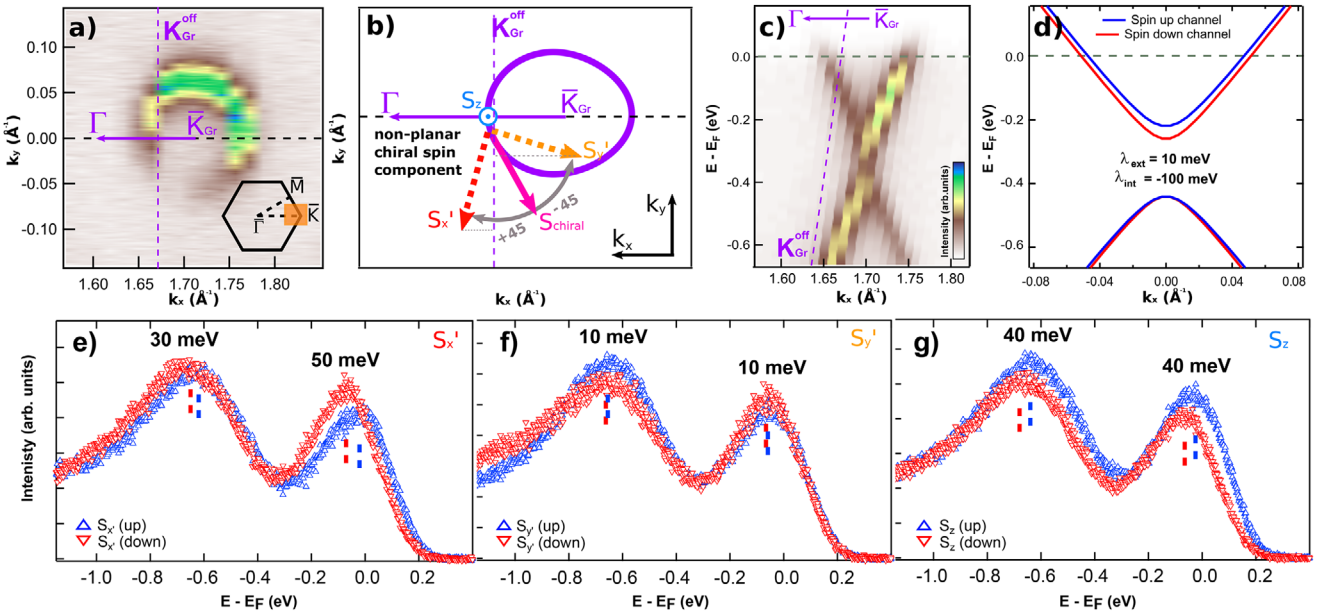

Figure 5. ARPES and SR-ARPES study of the 4/9 ML heterostructure at RT: gap opening and non-planar quasi-chiral spin texture of the gapped Gr Dirac cone. a) Experimental FS around $\overline{K}_{Gr}$ point. The inset indicates the measured portion of the SBZ. The vertical purple dashed line corresponds to the momentum at which SR-ARPES measurements were recorded and is coincident with the quantization axis for in-plane spin measurements, while the horizontal one indicates the direction for the ARPES bandmap shown in panel (c). b) Schematic of the FS illustrating the SR-ARPES measurement process using the spin rotator lens system (red and yellow arrows, see Experimental Section). The quasi-chiral in-plane spin component (fuchsia arrow) and positive out-of-plane spin polarization (blue) are consistent with the energy spin splitting detected in the SR-EDCs shown in panels (e–g). c) ARPES bandmap along the $\overline{\Gamma K}$ direction. (d) Band dispersion modeled using equation 1 (see main text for details). e–g) SR-EDCs for: e) in-plane S*x*′ (red arrow in panel (b)); f) in-plane S*y*′ (yellow arrow in panel (b)); and g) out-of-plane S*z* (blue arrow in panel (b)). Spin-up and spin-down components are represented by blue and red curves, respectively. Energy spin splittings, obtained from SR-EDC fitting, are indicated by dashed blue and red ticks.

Equation 1 has been parameterized to reproduce the experimental band dispersion, bandgap (Figures 3c and 5c), and in-plane energy spin splitting around $\overline{K}_{Gr}$ (Figure 5e). Using the experimentally determined $E_{DP} = -340$ meV and SOI strengths of $\lambda_{ext} = 10$ meV and $\lambda_{int} = -100$ meV the model reproduces the observed electronic structure. The resulting band dispersion from this semi-empirical approach is displayed in Figure 5d. This model considers the higher energy spin splitting of π^* states as compared to π states. The parametrization yields a spin splitting of 60 meV for the π^* states, close to the experimental data (Figure 5e). As a larger intrinsic SOI is considered, $|\lambda_{int}| > |\lambda_{ext}|$, the resulting nontrivial energy gap is $2(|\lambda_{int}| - |\lambda_{ext}|) = 2 \cdot (100 - 10) = 180$ meV. Therefore, both the bandgap and the energy spin splitting are well described by the model, and are consistent with previously reported systems such as Pb intercalated between Gr and Pt(111).[21]

Gr sublattice symmetry breaking, as mentioned in the Introduction section, can lead to a bandgap opening. However, in such a case, neither in-plane nor out-of-plane spin dependence should be observed, as in the case of Bi intercalation on Gr/Ir(111).[18] From the structural analysis based on LEED and STM (Figure 1) and assuming that the Gr lattice constant remains unchanged upon Te intercalation, the superstructures of intercalated Te are found to be commensurate with the underlying Ir(111) but not with the Gr layer. This rules out sublattice symmetry breaking as the origin of the bandgap emergence, unlike Gr/Bi/Ir(111) systems.[18,19] Accordingly, the sublattice symmetry should be preserved, as in Pb-intercalated systems.[21,22] This conclusion is further supported by the absence of an intravalley backscattering signature (a central ring with a radius of $2k_F$ at the Γ point) in the FFT images shown in Figure 2b.[64]

It is also important to consider the possible role played by the substrate in this case. The interaction between Ir(111) electronic states, mediated by states from the intercalated layer, and the Gr π bands may contribute to the emergence of SOI effects in the Dirac cone.[71] Nevertheless, the central role of Te intercalation must be emphasized, since Gr/Ir(111) alone exhibits nearly charge-neutral, quasi-free-standing Gr characteristics (see Figure S10, Supporting Information).[68,71]

A direct comparison with related intercalated systems based on outer-shell *p* elements highlights the distinctiveness of the Gr/Te/Ir(111) heterostructure. In the case of Sn and Sb intercalation, the resulting structures behave as quasi-free-standing Gr, without evidence of bandgap opening, SOI induction, or significant doping.[53,72] Bi intercalation does lead to a gap and doping, but SR-ARPES measurements show no spin splitting, indicating a sublattice symmetry breaking origin rather than SOI.[18] For Pb, an SOI-induced gap has been reported in Gr/Pb/Pt(111), although the structural interface suffers from rotational disorder;[21] meanwhile, in Gr/Pb/Ir(111), no measurable gap is observed, as intrinsic and extrinsic Rashba SOI are comparable.[22] In contrast, the Gr/Te/Ir(111) system uniquely combines high-quality epitaxial growth, a tunable SOI-induced bandgap with spin splitting, robust doping control. These results

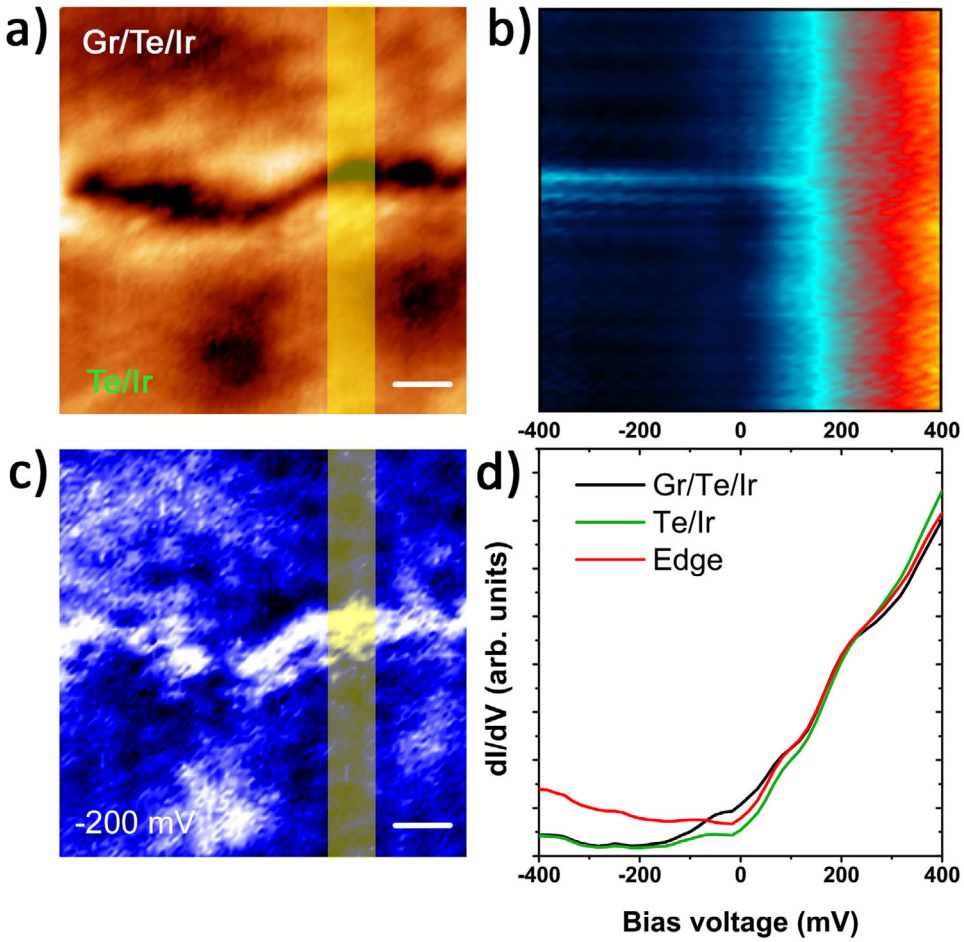

Figure 6. Edge states measured by STS. a) STM image taken at the boundary between Gr/Te/Ir and Te/Ir regions. b) 2D dI/dV plot averaging the area indicated in yellow in (a). c) dI/dV map taken at −200 mV. d) STS spectra taken at the different regions of (a).

suggest that the full heterostructure plays a cooperative role in enabling the observed phenomena.

2.4. Edge State

The emergence of a spin-orbit induced bandgap suggests the potential for the formation of a QSH phase. To investigate this, the presence of topologically non-trivial edge states within the bulk insulating gap is analyzed. STM has been employed to probe the topological behavior in several predicted QSH insulators, including WTe_2,[54] WSe_2,[73] bismuthene,[74] and $Bi_{14}Rh_3I_9$.[75]

For this experiment, a sub-monolayer of Gr was grown on Ir(111), and a low coverage of Te (1/3 ML phase) was intercalated, following the same procedure used for a full Gr ML (see Experimental Section and Figure S4, Supporting Information). After Te intercalation, the Te atoms formed a $(\sqrt{3}\times\sqrt{3})^\circ$ structure on the Ir patches. **Figure 6**a shows an STM image taken at the boundary between a Gr/Te/Ir region and a Te/Ir region, with the corresponding STS spectra at different positions depicted in Figure 6d. As expected for the low Te coverage regime, a decrease in the dI/dV signal is observed close to the Fermi level. In addition, an increase in the dI/dV signal appears at the edge under negative bias. This increase is more evident in the dI/dV maps taken at −200 mV and the 2D STS plot as a function of energy, taken along the yellow window marked in Figure 6a–c. In the plot, the enhancement of conductance within the gap at the edge is more evident, extending from the Fermi level to negative bias.

The observation of edge conductance alone does not suffice to confirm the presence of a QSH phase. However, the combination of several experimental findings–namely the conservation of sublattice symmetry, the observation of a significant bandgap, and the dominance of intrinsic SOI over Rashba-type SOI–strongly suggests the existence of a QSH phase in the Gr/Te/Ir(111) system.

3. Conclusion

In this work, Te has been effectively intercalated in Gr/Ir(111). Depending on the Te coverage, two distinct phases have been structurally resolved, both commensurate with the underlying Ir(111) substrate. Remarkably, a bandgap opens at the DP of Gr at RT, independent of the structural phase, while the relativistic dispersion of Gr remains unaffected. The origin of the bandgap has been attributed to a substantial intrinsic SOI that exceeds the extrinsic Rashba contribution. The DP has also been shown to

be tunable towards the Fermi energy by controlling the amount of intercalated Te, while preserving the bandgap. These findings pave the way for the development of innovative electronic and spintronic devices, as Te intercalation in Gr/Ir(111) provides a promising platform for tailoring spin-orbit coupling properties, including the possibility of generating a bandgap or inducing electronic doping. Finally, our work suggests that, in this system, transport properties near the DP are dominated by charge carriers of a single spin component. This indicates the potential of this system as a platform for realizing spin-dependent transport phenomena, such as the QSH effect. Replicating these structures and preserving their electronic properties on insulating substrates is therefore crucial for realizing their full application potential.

4. Experimental Section

Growth and Preparation Methods: Samples were prepared onto a Ir (111) monocrystal subjected to several sputtering-annealing cycles prior to the Gr deposition. A Gr ML was grown on Ir(111) by ethylene chemical vapor deposition at 1450 K with a total dose of 108 L followed by a post-annealing at 1443 K for 1 min. As a result, a high quality Gr layer of a single rotational phase was obtained as indicated by the LEED and STM images in Figures S1a, S2, and S3, Supporting Information. Sub-ML Gr was grown by exposing the Ir(111) surface to 36 L of ethylene with the substrate at RT, followed by an annealing at 1443 K for 10 min, see Figure S4, Supporting Information. Tellurium was deposited onto Gr/Ir(111) at RT using a Knudsen cell heated to $T_{Te} = 613$ K, with deposition times ranging from 4 to 10 min. After that, an annealing at 483 K for 5 min was applied in order to promote the intercalation process, confirmed by the recorded LEED patterns in Figure 1a,e. The characterization by LEED and STM revealed equivalent structures for the low (1/3 ML) and medium Te (4/9 ML) coverage samples, whereas different doping levels were observed in the ARPES experiments.

STM Experiments: STM measurements were performed in two UHV systems equipped with a low temperature STM (LT-STM) and a Joule-Thompson STM (JT-STM), respectively. STM images were recorded in constant current mode at RT, 77 K, 4.2 K or 1.2 K. The QPI maps were taken using a lock-in amplifier (f = 763 Hz) and their corresponding Fourier transforms have been symmetrized to improve the signal to noise ratio. The data were processed using the WSxM software.[76]

ARPES Experiments: ARPES experiments were carried out at the Spin-ARPES laboratory at IMDEA Nanociencia. Samples were previously characterized by STM and then transferred to the ARPES chamber by means of a UHV suitcase, being always kept at pressures better than 10^{-8} mbar. The analysis chamber was at RT and at a base pressure better than 10^{-10} mbars. ARPES measurements were performed with a He lamp with photon energy $h\nu = 21.2$ eV and a Specs Phoibos 150 hemispherical energy analyzer, with an acceptance angle of ±10° at Medium Angle Mode and ± 15° at Wide Angle Mode, providing an angular resolution better than 0.05° (0.002 $Å^{-1}$) and 0.075° (0.003 $Å^{-1}$), respectively for the short and long energy range maps, and an energy resolution of 80 meV.

SR-ARPES Experiments: SR-ARPES experiments were carried out at the Spin-ARPES laboratory at IMDEA Nanociencia. SR-ARPES measurements were recorded with a Combined Out-of-plane Specs 3D Micro-Mott/2D-CCD detector analyzer, which allows for the simultaneous measurement of the three spin components. Two orthogonal in-plane spin components can be measured by an implemented spin rotator lens system, which rotates ±45° the in-plane spins: with rotator lens $+45°_{(+1)}$ channels 1 and 2 measure one in-plane component (e.g., $S_{x'}$), and channeltrons 3 and 4 detect the out-of-plane one (S_z); whereas for the $-45°_{(-1)}$ rotator lens it was the remaining in-plane component ($S_{y'}$) the one which was detected in channels 1 and 2, while channels 3 and 4 redundantly detect the out-of-plane (S_z) signal. A circular aperture for the spin-transfer lens of 3 mm, and a pass energy of 10 eV were used, which gave rise to energy and angular (momentum) resolutions of 75 meV and 2.25° (0.06 $Å^{-1}$).[77] The spin up and spin down components were calculated from the results obtained from the normalized spectra in Figure S7, Supporting Information, by means of Equations (2) and (3):

$$I_{\uparrow} = (1 + P_{in(out)}) \cdot \frac{I_{in(out)}}{2} \quad (2)$$

$$I_{\downarrow} = (1 - P_{in(out)}) \cdot \frac{I_{in(out)}}{2} \quad (3)$$

where $P_{in(out)}$ is the spin polarization, defined as:

$$P_{in(out)} = \frac{A_{meas}}{S_{eff}} \quad (4)$$

being A_{meas} the measured spin asymmetry, and S_{eff} the Sherman function, which in this experimental setup amounts for 0.16.

DFT calculations: Density functional theory calculations were carried out within the projector augmented wave (PAW) approach,[78] as implemented in the VASP code,[79–81] using the Perdew-Burke-Ernzerhof (PBE) exchange correlation functional[82] and the Tkatchenko-Scheffler[83] corrections, to account for weak dispersion forces. A 400 eV plane wave cut-off and a total energy threshold of 10^{-5} eV for the self consistent field calculations were adopted. Depending on the size of the in-plane unit cell, the BZ sampling was carried out using unshifted Monkhorst-Pack grids,[84] ensuring a $\Delta k \lesssim 0.1$ Å. The Ir surface was modeled by 6-layer-thick Ir(111) slabs. Different amounts of intercalated Te were studied (see Supporting Information for further information) by placing the Te atoms on one side of the slab and a flat and stretched (so that the Gr lattice vectors matched the Ir(111) lattice vectors) Gr layer on top of it. In all cases a vacuum region of, at least, 20 Å in the out of plane direction was adopted. The final geometries were obtained relaxing the coordinates of the Gr atoms, the Te atoms, and the topmost two Ir layers until the maximum force was less than 0.01 eV $Å^{-1}$. The band plots shown in Figures S8 and S9 (Supporting Information) were obtained calculating the Kohn-Sham one electron energies and wavefunction over the usual BZ path of Gr. Each electron state was assigned a weight calculated as its overlap with the the wave function of a perfectly flat and accordingly stretched Gr layer. This procedure, in one go, singled out the Gr derived states and allowed to get rid of the replicated band due to the band folding, typical of the supercell calculations.[85]

Supporting Information

Supporting Information is available from the Wiley Online Library or from the author.

Acknowledgements

The authors thank Alireza Amiri for his assistance during the STM measurements. This work was supported by the Spanish Ministry of Science and Innovation, Grants no. PID2021-123776NB-C21 (CONPHASETM), PGC2018-098613-B-C21 (SpOrQuMat), EQC2019-006304-P (Equipamiento Científico), PID2020-116181RB-C31 (SOnanoBRAIN), PID2021-128011NB-I00, PID2021-123295NB-I00, and PID2019-105458RB-I00. IMDEA Nanociencia and IFIMAC acknowledge financial support from the Spanish Ministry of Science and Innovation through "Severo Ochoa" (Grant CEX2020-001039-S) and "María de Maeztu" (Grant CEX2018-000805-M) Programmes for Centres of Excellence in R&D, respectively. Financial support through the (MAD2D-CM)-MRR MATERIALES AVANZADOS-IMDEA-NC, (MAD2D-CM) MRR MATERIALES AVANZADOS-UAM and "Soluciones sostenibles del NanoMAGnetismo para TIC" (Mag4TIC-CM) is acknowledged. The authors acknowledge the funding from the EMPIR Programme co-financed by the Participating States and the European and Union's Horizon 2020 Research and Innovation Programme (grant EMPIR 20FUN03 COMET).

M.G. has received financial support through the "Ramón y Cajal" Fellowship program (RYC2020-029317-I) and "Ayudas para Incentivar la Consolidación Investigadora" (CNS2022-135175). M.G.C. acknowledges funding from the European Union's Horizon 2020 research and innovation programme under the Marie Skłodowska-Curie grant agreement no. 101034431 (IDEAL programme). M.G.C. is now at the Catalan Institute of Nanoscience and Nanotechnology (ICN2)

Conflict of Interest

The authors declare no conflict of interest.

Data Availability Statement

The data that support the findings of this study are available from the corresponding author upon reasonable request.

Keywords

angle-resolved photoemission spectroscopy, bandgap opening, graphene heterostructures, scanning tunneling microscopy, spin-orbit coupling

Received: December 19, 2024
Revised: April 23, 2025
Published online:

[1] S. Bae, H. Kim, Y. Lee, X. Xu, J.-S. Park, Y. Zheng, J. Balakrishnan, T. Lei, H. R. Kim, Y. I. Song, Y.-J. Kim, K. S. Kim, B. Ozyilmaz, J.-H. Ahn, B. H. Hong, S. Iijima, *Nat. Nanotechnol.* **2010**, *5*, 574.
[2] J. Ryu, Y. Kim, D. Won, N. Kim, J. S. Park, E.-K. Lee, D. Cho, S.-P. Cho, S. J. Kim, G. H. Ryu, H.-A-S. Shin, Z. Lee, B. H. Hong, S. Cho, *ACS Nano* **2014**, *8*, 950.
[3] A. Avsar, H. Ochoa, F. Guinea, B. Özyilmaz, B. J. van Wees, I. J. Vera-Marun, *Rev. Mod. Phys.* **2020**, *92*, 021003.
[4] N. Peres, *Rev. Mod. Phys.* **2010**, *82*, 2673.
[5] G. Fiori, F. Bonaccorso, G. Iannaccone, T. Palacios, D. Neumaier, A. Seabaugh, S. K. Banerjee, L. Colombo, *Nat. Nanotechnol.* **2014**, *9*, 768.
[6] W. Han, R. K. Kawakami, M. Gmitra, J. Fabian, *Nat. Nanotechnol.* **2014**, *9*, 794.
[7] B. Dlubak, M.-B. Martin, C. Deranlot, B. Servet, S. Xavier, R. Mattana, M. Sprinkle, C. Berger, W. A. De Heer, F. Petroff, A. Anane, P. Seneor, A. Fert, *Nat. Phys.* **2012**, *8*, 557.
[8] F. Ajejas, A. Gudín, R. Guerrero, A. Anadon Barcelona, J. M. Diez, L. de Melo Costa, P. Olleros, M. A. Niño, S. Pizzini, J. Vogel, M. Valvidares, P. Gargiani, M. Cabero, M. Varela, J. Camarero, R. Miranda, P. Perna, *Nano Lett.* **2018**, *18*, 5364.
[9] A. Chaves, J. G. Azadani, H. Alsalman, D. Da Costa, R. Frisenda, A. Chaves, S. H. Song, Y. D. Kim, D. He, J. Zhou, Jiadong Zhou, A. Castellanos-Gomez, F. M. Peeters, Z. Liu, C. L. Hinkle, S.-H. Oh, P. D. Ye, S. J. Koester, Y. H. Lee, Ph. Avouris, X. Wang, T. Low, *NPJ 2D Mater. Appl.* **2020**, *4*, 1.
[10] R. Balog, B. Jørgensen, L. Nilsson, M. Andersen, E. Rienks, M. Bianchi, M. Fanetti, E. Lægsgaard, A. Baraldi, S. Lizzit, Z. Sljivancanin, F. Besenbacher, B. Hammer, T. G. Pedersen, P. Hofmann, L. Hornekær, *Nat. Mater.* **2010**, *9*, 315.
[11] M. Sprinkle, M. Ruan, Y. Hu, J. Hankinson, M. Rubio-Roy, B. Zhang, X. Wu, C. Berger, W. A. De Heer, *Nat. Nanotechnol.* **2010**, *5*, 727.
[12] M. Papagno, S. Rusponi, P. M. Sheverdyaeva, S. Vlaic, M. Etzkorn, D. Pacilé, P. Moras, C. Carbone, H. Brune, *ACS Nano* **2012**, *6*, 199.
[13] Y.-W. Son, M. L. Cohen, S. G. Louie, *Nature* **2006**, *444*, 347.
[14] A. L. Vázquez de Parga, F. Calleja, B. Borca, M. Passeggi Jr, J. Hinarejos, F. Guinea, R. Miranda, *Phys. Rev. Lett.* **2008**, *100*, 056807.
[15] F. Yavari, C. Kritzinger, C. Gaire, L. Song, H. Gulapalli, T. Borca-Tasciuc, P. M. Ajayan, N. Koratkar, *Small* **2010**, *6*, 2535.
[16] S. Y. Zhou, G.-H. Gweon, A. Fedorov, d. First, PN, W. De Heer, D.-H. Lee, F. Guinea, A. Castro Neto, A. Lanzara, *Nat. Mater.* **2007**, *6*, 770.
[17] C. Enderlein, Y. Kim, A. Bostwick, E. Rotenberg, K. Horn, *New J. Phys.* **2010**, *12*, 033014.
[18] M. Krivenkov, D. Marchenko, J. Sánchez-Barriga, E. Golias, O. Rader, A. Varykhalov, *2D Mater.* **2021**, *8*, 035007.
[19] J. Warmuth, A. Bruix, M. Michiardi, T. Hänke, M. Bianchi, J. Wiebe, R. Wiesendanger, B. Hammer, P. Hofmann, A. A. Khajetoorians, *Phys. Rev. B* **2016**, *93*, 165437.
[20] A. Bostwick, T. Ohta, J. L. McChesney, K. V. Emtsev, T. Seyller, K. Horn, E. Rotenberg, *New J. Phys.* **2007**, *9*, 385.
[21] I. I. Klimovskikh, M. M. Otrokov, V. Y. Voroshnin, D. Sostina, L. Petaccia, G. Di Santo, S. Thakur, E. V. Chulkov, A. M. Shikin, *ACS Nano* **2017**, *11*, 368.
[22] M. M. Otrokov, I. I. Klimovskikh, F. Calleja, A. M. Shikin, O. Vilkov, A. G. Rybkin, D. Estyunin, S. Muff, J. H. Dil, A. L. Vázquez de Parga, R. Miranda, H. Ochoa, F. Guinea, J. I. Cerdá, E. V. Chulkov, A. Arnau, *2D Mater.* **2018**, *5*, 035029.
[23] F. Calleja, H. Ochoa, M. Garnica, S. Barja, J. J. Navarro, A. Black, M. M. Otrokov, E. V. Chulkov, A. Arnau, A. L. Vázquez de Parga, F. Guinea, R. Miranda, *Nat. Phys.* **2015**, *11*, 43.
[24] D. Ma, Z. Yang, *New J. Phys.* **2011**, *13*, 123018.
[25] S. Bader, S. Parkin, *Annu. Rev. Condens. Matter Phys.* **2010**, *1*, 71.
[26] C. L. Kane, E. J. Mele, *Phys. Rev. Lett.* **2005**, *95*, 146802.
[27] C. L. Kane, E. J. Mele, *Phys. Rev. Lett.* **2005**, *95*, 226801.
[28] M. Z. Hasan, C. L. Kane, *Rev. Mod. Phys.* **2010**, *82*, 3045.
[29] X.-L. Qi, S.-C. Zhang, *Rev. Mod. Phys.* **2011**, *83*, 1057.
[30] E. I. Rashba, *Phys. Rev. B* **2009**, *79*, 161409.
[31] A. Castro Neto, F. Guinea, *Phys. Rev. Lett.* **2009**, *103*, 026804.
[32] Z. Qiao, S. A. Yang, W. Feng, W.-K. Tse, J. Ding, Y. Yao, J. Wang, Q. Niu, *Phys. Rev. B* **2010**, *82*, 161414.
[33] J. Sánchez-Barriga, A. Varykhalov, M. Scholz, O. Rader, D. Marchenko, A. Rybkin, A. Shikin, E. Vescovo, *Diam. Relat. Mater.* **2010**, *19*, 734.
[34] J. Boettger, S. Trickey, *Phys. Rev. B* **2007**, *75*, 121402.
[35] H. Min, J. E. Hill, N. A. Sinitsyn, B. R. Sahu, L. Kleinman, A. H. MacDonald, *Phys. Rev. B* **2006**, *74*, 165310.
[36] Y. Yao, F. Ye, X.-L. Qi, S.-C. Zhang, Z. Fang, *Phys. Rev. B* **2007**, *75*, 041401.
[37] J. F. Sierra, J. Fabian, R. K. Kawakami, S. Roche, S. O. Valenzuela, *Nature Nanotechnology* **2021**, *16*, 856.
[38] M. Gmitra, D. Kochan, P. Högl, J. Fabian, *Phys. Rev. B* **2016**, *93*, 155104.
[39] K. Zollner, J. Fabian, *Physica Status Solidi (b)* **2021**, *258*, 2000081.
[40] P. Tiwari, M. K. Jat, A. Udupa, D. S. Narang, K. Watanabe, T. Taniguchi, D. Sen, A. Bid, *npj 2D Materials and Applications* **2022**, *6*, 68.
[41] Y. Dedkov, E. Voloshina, *J. Condens. Matter Phys.* **2015**, *27*, 303002.
[42] E. Voloshina, Y. S. Dedkov, *Mater. Res. Express* **2014**, *1*, 035603.
[43] I. I. Klimovskikh, O. Vilkov, D. Y. Usachov, A. Rybkin, S. Tsirkin, M. Filianina, K. Bokai, E. Chulkov, A. Shikin, *Phys. Rev. B* **2015**, *92*, 165402.
[44] H. Vita, S. Böttcher, K. Horn, E. Voloshina, R. Ovcharenko, T. Kampen, A. Thissen, Y. S. Dedkov, *Sci. Rep.* **2014**, *4*, 1.
[45] H. Zhang, C. Lazo, S. Blügel, S. Heinze, Y. Mokrousov, *Phys. Rev. Lett.* **2012**, *108*, 056802.
[46] J. Hu, J. Alicea, R. Wu, M. Franz, *Phys. Rev. Lett.* **2012**, *109*, 266801.
[47] A. M. Shikin, A. G. Rybkin, D. Marchenko, A. A. Rybkina, M. R. Scholz, O. Rader, A. Varykhalov, *New J. Phys.* **2013**, *15*, 013016.

[48] D. Marchenko, J. Sánchez-Barriga, M. Scholz, O. Rader, A. Varykhalov, *Phys. Rev. B* **2013**, *87*, 115426.
[49] A. Varykhalov, J. Sánchez-Barriga, D. Marchenko, P. Hlawenka, P. Mandal, O. Rader, *Nat. Commun.* **2015**, *6*, 1.
[50] P. Sheverdyaeva, G. Bihlmayer, E. Cappelluti, D. Pacile, F. Mazzola, N. Atodiresei, M. Jugovac, I. Grimaldi, G. Contini, A. K. Kundu, I. Vobornik, J. Fujii, P. Moras, C. Carbone, L. Ferrari, *Phys. Rev. Lett.* **2024**, *132*, 266401.
[51] L. Brey, *Phys. Rev. B* **2015**, *92*, 235444.
[52] N. Briggs, B. Bersch, Y. Wang, J. Jiang, R. J. Koch, N. Nayir, K. Wang, M. Kolmer, W. Ko, A. De La Fuente Duran, J. Shallenberger, M. Fu, Q. Zou, Y.-W. Chuang, Z. Gai, A.-P. Li, A. Bostwick, C. Jozwiak, C.-Z. Chang, E. Rotenberg, J. Zhu, A. C. T. van Duin, V. Crespi, J. A. Robinson, *Nat. Mater.* **2020**, *19*, 637.
[53] Y.-R. Lin, S. Wolff, P. Schädlich, M. Hutter, S. Soubatch, T.-L. Lee, F. S. Tautz, T. Seyller, C. Kumpf, F. C. Bocquet, *Phys. Rev. B* **2022**, *106*, 155418.
[54] S. Tang, C. Zhang, D. Wong, Z. Pedramrazi, H. Z. Tsai, C. Jia, B. Moritz, M. Claassen, H. Ryu, S. Kahn, J. Jiang, H. Yan, M. Hashimoto, D. Lu, R. G. Moore, C. C. Hwang, C. Hwang, Z. Hussain, Y. Chen, M. M. Ugeda, Z. Liu, X. Xie, T. P. Devereaux, M. F. Crommie, S. K. Mo, Z. X. Shen, *Nat. Phys.* **2017**, *13*, 683.
[55] R. Roldan, M. P. López-Sancho, F. Guinea, E. Cappelluti, J. A. Silva-Guillén, P. Ordejon, *2D Mater.* **2014**, *1*, 034003.
[56] A. Avsar, J. Y. Tan, T. Taychatanapat, J. Balakrishnan, G. Koon, Y. Yeo, J. Lahiri, A. Carvalho, A. Rodin, E. O'Farrell, G. Eda, A. H. Castro Neto, B. Özyilmaz, *Nat. Commun.* **2014**, *5*, 1.
[57] G. Qiu, A. Charnas, C. Niu, Y. Wang, W. Wu, P. D. Ye, *NPJ 2D Mater. Appl.* **2022**, *6*, 17.
[58] R. Bernardo Gavito, Intercalation of sulfur in epitaxial graphene on ruthenium (0001) studied by means of scanning tunneling microscopy and spectroscopy. Ph.D. thesis, Universidad Autónoma de Madrid, **2016**, https://repositorio.uam.es/handle/10486/672150.
[59] M. Pisarra, R. Bernardo-Gavito, J. Navarro, A. Black, C. Díaz, F. Calleja, D. Granados, R. Miranda, F. Martín, A. L. Vázquez de Parga, *Appl. Surf. Sci.* **2018**, *433*, 300.
[60] M. Pisarra, C. Díaz, R. Bernardo-Gavito, J. J. Navarro, A. Black, F. Calleja, D. Granados, R. Miranda, A. L. Vázquez de Parga, F. Martín, *J. Phys. Chem. A* **2018**, *122*, 2232.
[61] I. Brihuega, P. Mallet, C. Bena, S. Bose, C. Michaelis, L. Vitali, F. Varchon, L. Magaud, K. Kern, J. Y. Veuillen, *Physical Review Letters* **2008**, *101*, 206802.
[62] G. Rutter, J. Crain, N. P. Guisinger, T. Li, P. First, J. Stroscio, *Science* **2007**, *317*, 219.
[63] Y. Cui, H. Zhang, W. Chen, Z. Yang, Q. Cai, *The Journal of Physical Chemistry C* **2017**, *121*, 15282.
[64] P. Mallet, I. Brihuega, S. Bose, M. M. Ugeda, J. M. Gómez-Rodróguez, K. Kern, J. Y. Veuillen, *Phys. Rev. B* **2012**, *86*, 04544.
[65] M. F. Crommie, C. P. Lutz, D. M. Eigler, *Nature* **1993**, *363*, 524.
[66] Y. Hasegawa, P. Avouris, *Phys. Rev. Lett.* **1993**, *71*, 1071.
[67] K. Miyamoto, A. Kimura, T. Okuda, H. Miyahara, K. Kuroda, H. Namatame, M. Taniguchi, S. Eremeev, T. V. Menshchikova, E. V. Chulkov, K. A. Kokh, O. E. Tereshchenko, *Phys. Rev. Lett.* **2012**, *109*, 166802.
[68] M. Kralj, I. Pletikosić, M. Petrović, P. Pervan, M. Milun, A. T. N'Diaye, C. Busse, T. Michely, J. Fujii, I. Vobornik, *Phys. Rev. B* **2011**, *84*, 075427.
[69] S. Abdelouahed, A. Ernst, J. Henk, I. Maznichenko, I. Mertig, *Phys. Rev. B* **2010**, *82*, 125424.
[70] M. Gmitra, S. Konschuh, C. Ertler, C. Ambrosch-Draxl, J. Fabian, *Phys. Rev. B* **2009**, *80*, 235431.
[71] B. Muñiz Cano, A. Gudín, J. Sánchez-Barriga, O. Clark, A. Anadón, J. M. Díez, P. Olleros-Rodríguez, F. Ajejas, I. Arnay, M. Jugovac, J. Rault, P. Le Fèvre, F. Bertran, D. Mazhjoo, G. Bihlmayer, O. Rader, S. Blügel, R. Miranda, J. Camarero, M. A. Valbuena, P. Perna, *ACS Nano* **2024**, *18*, 38847339.
[72] H. Kim, J. Kim, Y. Jung, B. H. Lee, J. Hwang, Y. J. Chang, *Journal of Physics D: Applied Physics* **2016**, *49*, 135307.
[73] M. M. Ugeda, A. Pulkin, S. Tang, H. Ryu, Q. Wu, Y. Zhang, D. Wong, Z. Pedramrazi, A. Martín-Recio, Y. Chen, F. Wang, Z. X. Shen, S. K. Mo, O. V. Yazyev, M. F. Crommie, *Nat. Commun.* **2018**, *9*, 1.
[74] F. Reis, G. Li, L. Dudy, M. Bauernfeind, S. Glass, W. Hanke, R. Thomale, J. Schöfer, R. Claessen, *Science* **2017**, *357*, 287.
[75] C. Pauly, B. Rasche, K. Koepernik, M. Liebmann, M. Pratzer, M. Richter, J. Kellner, M. Eschbach, B. Kaufmann, L. Plucinski, C. M. Schneider, M. Ruck, J. V. D. Brink, M. Morgenstern, *Nature Physics* **2015**, *11*, 338.
[76] I. Horcas, R. Fernández, J. M. Gómez-Rodríguez, J. Colchero, J. Gómez-Herrero, A. M. Baro, *Rev. Sci. Instrum.* **2007**, *78*, 013705.
[77] M. H. Berntsen, P. Palmgren, M. Leandersson, A. Hahlin, J. Åhlund, B. Wannberg, M. Månsson, O. Tjernberg, *Rev. Sci. Instrum.* **2010**, *81*, 035104.
[78] P. E. Blöchl, *Phys. Rev. B* **1994**, *50*, 17953.
[79] G. Kresse, D. Joubert, *Phys. Rev. B* **1999**, *59*, 1758.
[80] G. Kresse, J. Furthmüller, *Comput. Mater. Sci.* **1996**, *6*, 15.
[81] G. Kresse, J. Furthmüller, *Phys. Rev. B* **1996**, *54*, 11169.
[82] J. P. Perdew, K. Burke, M. Ernzerhof, *Phys. Rev. Lett.* **1996**, *77*, 3865.
[83] A. Tkatchenko, M. Scheffler, *Phys. Rev. Lett.* **2009**, *102*, 073005.
[84] H. J. Monkhorst, J. D. Pack, *Phys. Rev. B* **1976**, *13*, 5188.
[85] W. Ku, T. Berlijn, C.-C. Lee, *Phys. Rev. Lett.* **2010**, *104*, 216401.